Available online at www.sciencedirect.com
SCIENCE DIRECT®
Pergamon
Acta Materialia 51 (2003) 1211–1228
Acta MATERIALIA
www.actamat-journals.com

Laser-induced shock compression of monocrystalline copper: characterization and analysis

M.A. Meyers [a,*], F. Gregori [b], B.K. Kad [a], M.S. Schneider [a], D.H. Kalantar [c], B.A. Remington [c], G. Ravichandran [d], T. Boehly [e], J.S. Wark [f]

[a] *University of California, Department of Mechanical and Aerospace Engineering, Mail Code 0411 9500 Gilman Drive, San Diego, La Jolla, CA 92093-0411, USA*
[b] *University of Paris 13, Villetaneuse, France*
[c] *Lawrence Livermore National Laboratory, Livermore, CA, USA*
[d] *California Institute of Technology, Pasadena, CA, USA*
[e] *University of Rochester, Rochester, NY, USA*
[f] *University of Oxford, Oxford, UK*

Received 7 February 2002; accepted 27 August 2002

Abstract

Controlled laser experiments were used to generate ultra-short shock pulses of approximately 5 ns duration in monocrystalline copper specimens with [001] orientation. Transmission electron microscopy revealed features consistent with previous observations of shock-compressed copper, albeit at pulse durations in the μs regime. At pressures of 12 and 20 GPa, the structure consists primarily of dislocation cells; at 40 GPa, twinning and stacking-fault bundles are the principal defect structures; and at a pressure of 55–60 GPa, the structure shows micro-twinning and the effects of thermal recovery (elongated sub-grains). The results suggest that the defect structure is generated at the shock front; the substructures observed are similar to the ones at much larger durations. The dislocation generation is discussed, providing a constitutive description of plastic deformation. It is proposed that thermally activated loop nucleation at the front is the mechanism for dislocation generation. A calculational method for dislocation densities is proposed, based on nucleation of loops at the shock front and their extension due to the residual shear stresses behind the front. Calculated dislocation densities compare favorably with experimentally observed results. It is proposed that simultaneous diffraction by Laue and Bragg of different lattice planes at the shock front can give the strain state and the associated stress level at the front. This enables the calculation of the plastic flow resistance at the imposed strain rate. An estimated strength of 435 MPa is obtained, for a strain rate of 1.3×10^7 s^{-1}. The threshold stress for deformation twinning in shock compression is calculated from the constitutive equations for slip, twinning, and the Swegle–Grady relationship. The calculated threshold pressure for the [001] orientation is 16.3 GPa.
© 2003 Acta Materialia Inc. Published by Elsevier Science Ltd. All rights reserved.

Keywords: Twinning; Dynamic deformation; Plastic deformation; Copper; Laser; Shock

1. Introduction

Askaryon and Morez [1] demonstrated in 1963 that shock pulses could be generated in metals

* Corresponding author. Tel.: +1-858-534-4719; fax: +1-858-534-5698.
E-mail address: mameyers@mae.ucsd.edu (M.A. Meyers).

1359-6454/03/$30.00 © 2003 Acta Materialia Inc. Published by Elsevier Science Ltd. All rights reserved.
doi:10.1016/S1359-6454(02)00420-2

from laser-pulse induced vaporization at the surface. The use of surfaces covered by a laser-transparent overlay was introduced by Anderholm [2]; this enabled the confinement of the vapor products resulting in an increase of the peak pressure of the shock incident on the metal. Shock amplitudes as high as those generated by explosives or planar impact devices could be generated with a basic difference: the duration of the shock pulse was in the nanosecond range. Fairand et al. [3] and Clauer et al. [4] used these laser-induced shock pulses to modify the microstructure of engineering alloys, increasing their strength and fatigue resistance.

Simultaneous shock compression and X-ray diffraction experiments were introduced by Johnson et al. [5] and continued by Zaretsky et al. [6]. Wark et al. [7] used laser-generated X-rays to produce shock compression at the Nova laser facility. These shock compression experiments on silicon monocrystals were coupled with X-ray diffraction that successfully measured the compression both perpendicular (Laue) and parallel (Bragg) to the shock propagation direction. The X-rays that generated the shock pressure were created by eight laser beams focused into an internally shielded hohlraum [8], and the X-rays used for X-ray diffraction were provided by two lasers incident on a separate metal foil.

The use of simultaneous shock compression and X-ray diffraction offers a very attractive means of observing the distortions in the lattice as it is being compressed. These measurements are essential to unravel the mechanisms of plastic deformation in shock compression. A number of proposals for dislocation generation in shock compression have been advanced over the years [9–14], but none of them have been critically tested.

This paper describes a series of experiments carried out on copper single crystals at the Omega ICF (Inertial Confinement Fusion) Facility, University of Rochester. Some of these experiments were carried out to record the simultaneous Bragg and Laue diffraction, while others were carried out to shock compress and then recover the sample for post-mortem analysis of the plastic deformation microstructure. The initial shock amplitudes varied from approximately 10 to 60 GPa and pulse durations were on the order of 5 ns, one order of magnitude lower than earlier shock laser experiments (20–100 ns) and two orders of magnitude lower than plate impact experiments (0.1–0.2 μs). Thus, these experiments explore a new regime of shock compression. In this paper, we describe laser recovery experiments and the deformation substructures generated, and compare these observations with analytical predictions.

2. Experimental techniques

For the recovery experiments, single crystals of Cu with a [100] orientation were obtained from Goodfellow in the form of disks with 2.0–3.0 mm diameter and 1 mm thickness. They were mounted into foam-filled recovery tubes shown in Fig. 1(a). Foam with a density of 50 mg/cm^3 was used to decelerate the samples for recovery.

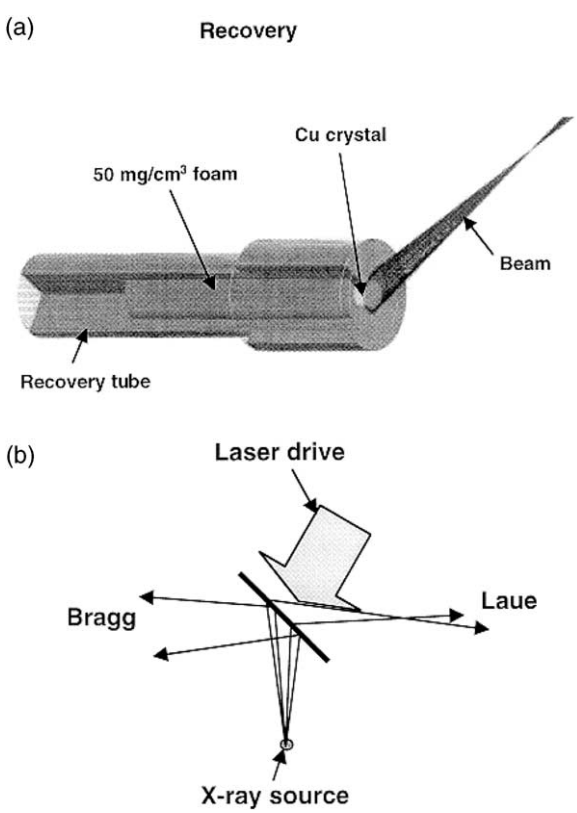

Fig. 1. (a) Sample and recovery tube; (b) set-up for shock compression and diffraction.

The shock amplitude at the surface of the Cu crystal can be obtained from the laser energy and the computed values (using hydrocode calculations). Results are shown in Fig. 2. In some experiments, a CH plastic layer was used as an ablator. This resulted in an impedance mismatch at the CH/Cu interface, which enhanced the shock pressure in the copper specimen. Due to the short duration of the shock created by the 3 ns laser pulse, the decay in the specimen is very rapid. This decay is calculated by a hydrodynamics code. Snapshots of the pressure profiles in the Cu at various times for the case of a 1 mm thick single crystal Cu are shown in Fig. 2(a), (b), and (c) for three initial laser energies, respectively: 40, 205 and 320 J. Fig. 2(d) shows the decay of the maximum pressure in the specimens at these three laser energies. It can be seen that there is significant decrease from the front to the back surface.

The results of four shock/recovery experiments are reported here: (a) energy = 40 J directly onto Cu; (b) energy = 70 J directly onto copper; (c) energy = 205 J directly onto Cu; (d) energy = 320 J onto a 20 μm CH ablator on Cu. These are compared with analysis of an unshocked crystal sample. The pressure ranges for these shocked samples are approximately 8–12, 18–25, 35–40, and 55–60 GPa near the shocked surface. Although the pressure decays throughout the specimens, these values are used in the following discussions.

Each of the 1 mm thick shocked specimens was sliced into two or three discs using a slow-speed diamond saw and ground mechanically to a thickness of 100 μm (see Fig. 3). Thin foils were prepared for TEM examination by using a twin-jet Fishione polisher with an electro-polishing solution composed by 7 vol.% of sulfuric acid in methanol. TEM was conducted in a Philips CM-30 microscope operating at 300 kV.

For the dynamic X-ray diffraction experiments, thin foils of single crystal copper were obtained from the Thin Film Laboratories in Denmark (J.

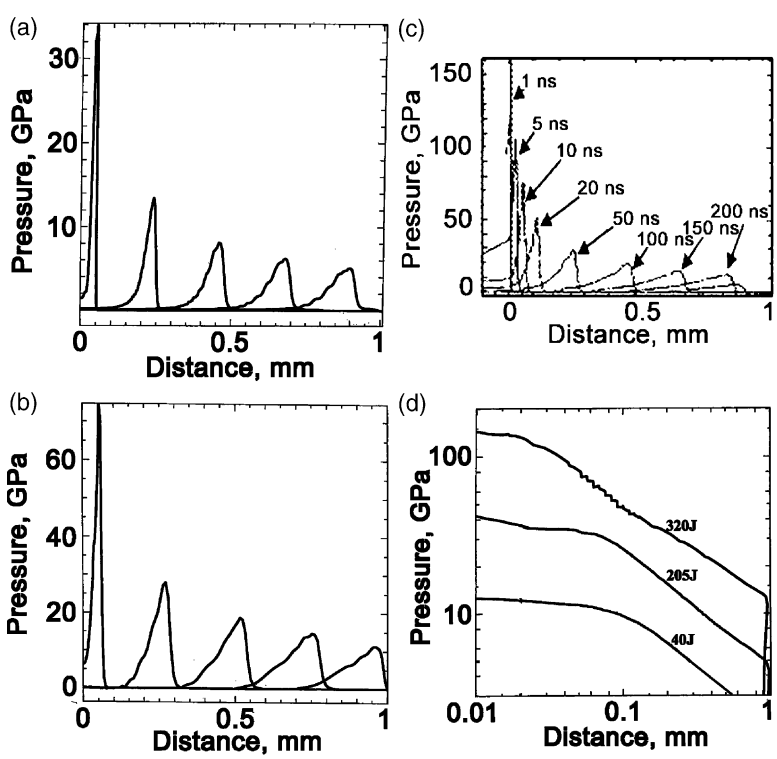

Fig. 2. Computed shock-wave profiles for laser energies of (a) 40 J; (b) 205 J; (c) 320 J; (d) Maximum pressure as a function of distance from irradiation surface for three shock conditions.

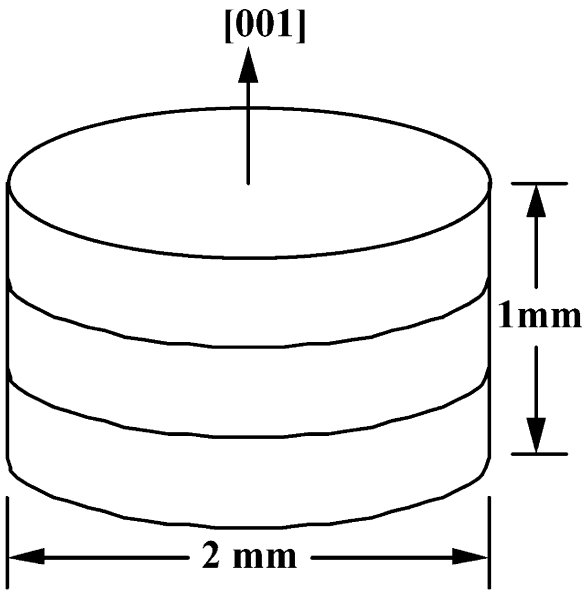

Fig. 3. Schematic showing the sectioning of the laser shocked specimens to create multiple thin foils for TEM observations.

Chevalier). These were 2–8 μm thick, with a [100] lattice orientation. A short duration high intensity laser beam irradiated the surface of the single crystal, ablating material and creating a shock that compressed the thin foil. Separate laser beams were used to generate 5.2 keV X-rays for X-ray diffraction. A 100 μm Ta pinhole was used as an aperture for the X-rays, creating a small (point) source for diffraction. These X-rays were then recorded in both transmission (Laue) and reflection (Bragg). The detectors were placed at the approximate angles to capture the diffracted {200} from Laue and Bragg. The X-ray source was located close to the shocked crystal such that X-rays were incident at a wide range of angles (Fig. 1(b)). The X-rays matched the Bragg angles for the (200) and (020) lattice planes for a range of lattice spacings. Therefore, we were able to record diffracted X-rays from both the unshocked lattice and the shock-compressed lattice. The changes in the spacing of these planes could be followed by the changes in the diffracted angles. Both time-integrated and time-resolved (streaked) observations were made.

3. Experimental results and discussion

Copper has been the object of numerous shock recovery experiments and its response is fairly well understood. It has a stacking-fault energy of 57 ± 8 mJ/m^2. The shock-induced structure consists of dislocation cells up to a critical pressure. At higher pressures, twinning is prevalent. For single crystals, De Angelis and Cohen [15] found that the crystal twinning stress was 14 GPa, for the shock wave propagating along [100] while it was 20 GPa for [111]. This is consistent with the findings by Nolder and Thomas [16,17] for nickel. Murr [18] and Grace [19] observed a cellular structure with the cell size decreasing from 0.7 μm at 5.5 GPa to 0.15 μm at 34.5 GPa.

In some of the shocked specimens examined here, there are systematic differences in the deformation substructures for the different energy inputs. However, for a given input energy, in some shocked specimens, we have observed rather dramatic changes in deformation substructure in the electron transparent regions surrounding the thin foil perforation. This is consistent with the area illuminated by the laser beam, which is on the order of the copper specimen area. It is also consistent with the fact that the laser energy is not spatially uniform, being highest at the center. For a nominal perforation of about 200 μm, the regions examined are typically 250 μm apart as measured. With this in mind we have taken specific steps to document the entire deformation substructure around the hole, perhaps indicative of the substructure variations implicit in such laser-shocked tests.

The unshocked copper crystal shows only a limited number of dislocations without preferred alignments or arrangements. The dislocation density is typically that of an un-deformed crystal.

3.1. Deformation microstructure of samples shocked at 12 GPa (40 J) and 20 GPa (70 J)

The 12 GPa shock creates a cellular organization with a medium density of 1/2<110> dislocations. The cell size appears homogeneous with average dimensions between 0.3–0.6 μm, as illustrated in Fig. 4(a). This deformation microstructure was similar on all sides of the perforation. In thicker

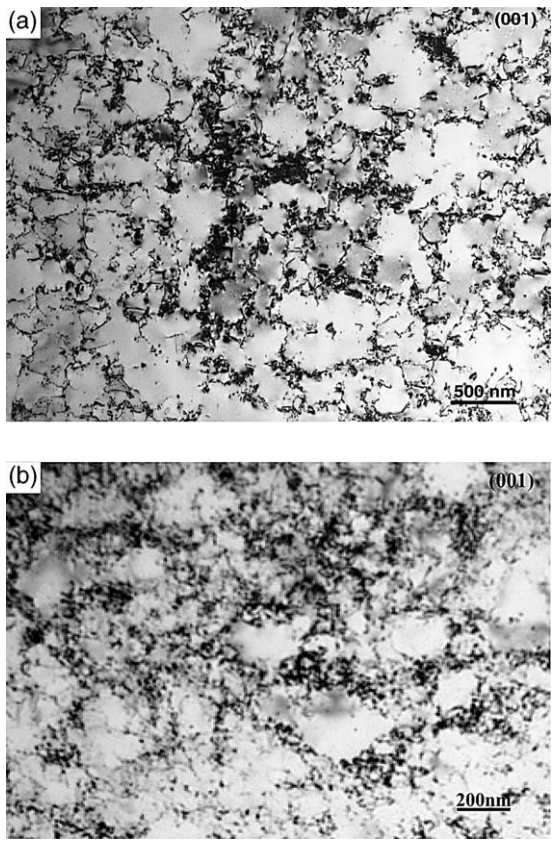

Fig. 4. Dislocation substructure for the Cu specimens shocked at (a) 40 J energy; the TEM electron beam direction is B = [001]; (b) 70 J energy; the TEM electron beam direction is B = [001].

areas, away from the perforation edge, the microstructure consists of dense dislocation cells. In areas near the perforation edge, the dislocation cells are not closed. The apparent variation in cell structure is therefore attributed to thickness effects of the thin foil.

The sample shocked at 20 GPa contained a similar microstructure to that shocked at 12 GPa (Fig. 4(b)). The shock creates a well-defined cellular organization of 1/2<110> dislocations with average dimensions between 0.2 and 0.3 μm cell size. The microstructure was homogeneous throughout the sample and included the previously described thickness effects.

Qualitatively, these results confirm previous observations, albeit at a pulse duration that is lower by a factor of 10–100 than that applied by Murr [18]. Fig. 5 shows a plot of that data. The predicted cell size from Murr's plot, at a pressure of 12 GPa, is 0.4 μm. The observed cell size is also consistent with Gray's [20] measurements: 0.5 μm/10 GPa. However, the dislocation density, i.e. cell-wall thickness, seems to be lower than in these previous studies.

One interesting feature is the observation of a large number of loops. For example, loops as small as 25 nm and as large as 250 nm are indicated in Fig. 6. Given the density of loops observed, far greater than that observed in undeformed Cu, it is reasonable to suggest that the loop nucleation is an essential event of the laser-induced shock compression. Another interesting feature at this pressure is the presence of isolated dislocations within the cells. These dislocations appear to be pinned on particles or defects that are not discernible at the resolution available in the present TEM observations.

3.2. Deformation microstructure of samples shocked at 40 GPa (205 J)

This intermediate energy input creates dense dislocation tangles, stacking faults, and micro-twins. There are no readily discernible dislocation cells. Furthermore, the observed deformation sub-struc-

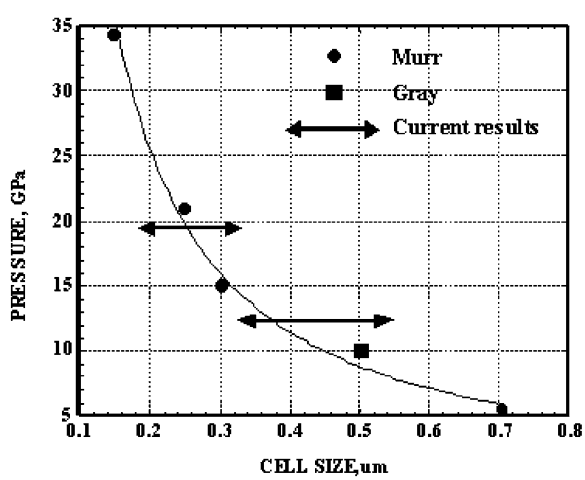

Fig. 5. Cell size as a function of pressure for shock loaded copper (adapted from Murr [18]).

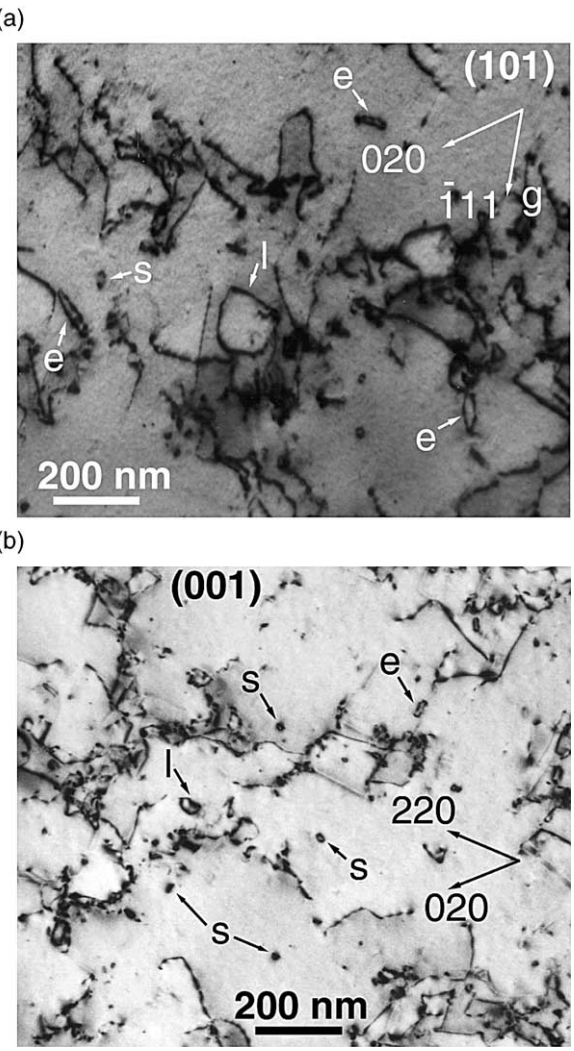

Fig. 6. Observation of numerous loops in the 40 J shocked specimens. The different sizes (l = large; s = small) and shapes (e = elongated) of the high density of loops are indicated in (a) where the TEM electron beam is B = [101] and (b) B = [001].

ture appears uniform around the thin foil perforation. These traces are characteristic of stacking-fault bundles and twins and are analogous to previous observations by Murr [21], especially Figs. 20, 21 and 23 of [21]. These features are significantly different than the ones at the lower energy. Perpendicular traces of planar features are seen when the TEM electron beam direction is B=<001>. These correspond to traces of {111} on (001). These traces have orientations <220>, as shown in Fig. 7a.

All four stacking fault variants viz the $(1\ 1\ \bar{1})1/6[112]$, $(111)1/6[1\ \bar{1}\ 2]$, $(1\ \bar{1}\ 1)1/6[1\ \bar{1}\ 2]$, and $(1\ \bar{1}\ 1)1/6[\bar{1}\ 1\ 2]$ are observed, indicated as A, B, C, and D in Fig. 7(a)-(c). Given the incident energy input as parallel to [001], it is not surprising that all four stacking fault variants are activated, Fig. 7(a), as they all have the same Schmid factor. However, there is a significant difference in the activation along $[\bar{2}\ 2\ 0]$ (SF: A, B) versus [2 2 0] (SF: C, D) with the density of occurrence significantly higher in the former, Fig. 7(b). For example, variant A is spaced approximately 230 nm apart. The C variant occurs less with a considerably wider (450 nm) spacing. Variants B and D are roughly equally spaced at 1 μm, with their activation far fewer than either A or C, Fig. 7(c). The smaller spacing and larger length of variant A seems to indicate that it formed first. Note that the SF variant C is often truncated between A-variant pairs (see Fig. 7(b)).

While not specifically indicated in the micrographs, a large number of small (about 10 nm) dislocation loops were observed. The isolated pinned dislocations point to some pinning events similar to the case in samples deformed at lower pressures (12 and 20 GPa).

3.3. Deformation microstructure of samples shocked at 55–60 GPa (320 J)

The deformation microstructure consists of a high density of micro-twins (Fig. 8) and laths (Fig. 9). The deformation is not uniform around the perforation, with the micro-twins situated closer to the center of the sample and the laths away from the center. Fig. 10 indicates the relative positions of these features.

Two sets of micro-twins (A and B) are observed in the thin foils (not shown here). When imaged at beam direction B = [0 0 1], they appear at exactly 90 degrees one to each other aligned along [2 2 0](set A) and $[\bar{2}\ 2\ 0]$(set B) directions, respectively, and they are present roughly in same proportion (not shown here). We will focus our description only on set A. When imaged in the edge orientation at the beam direction close to

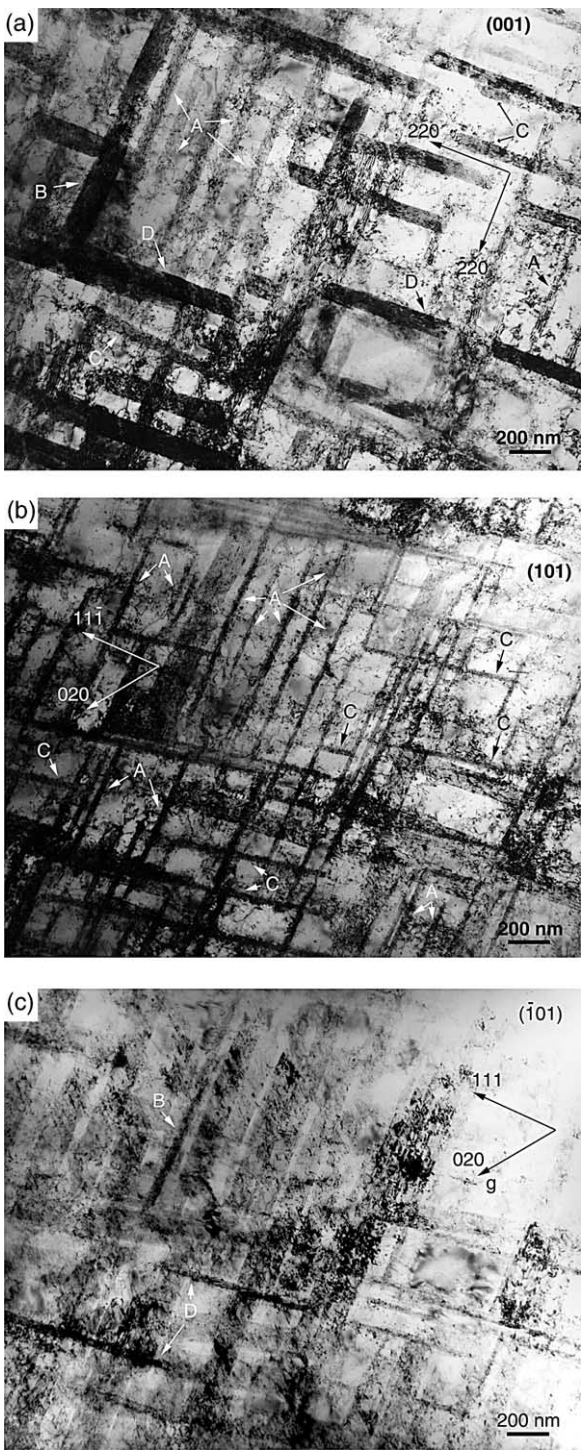

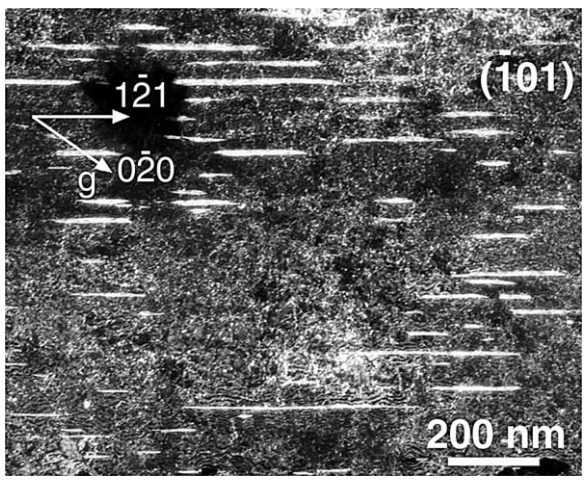

Fig. 8. Micro-twins with a (111) habit plane elongated along [1 $\bar{2}$ 1]. Energy input = 320 J, g = 0 $\bar{2}$ 0, beam direction B = [101].

[$\bar{1}$ 0 1], Fig. 8, the micro-twins from set A have the (1 1 1) habit plane and are elongated along [1 $\bar{2}$ 1]. This set of micro-twins exhibits a wide range of lengths, from as small as 70 nm to as large as 1 μm; the mean value is around 125 nm. In contrast, the set B micro-twins have a near uniform length of 70nm.

Unlike the micro-twins, the laths are elongated close to <2 2 0>. In some regions they are aligned along [2 2 0] and in others along [2 2 0]. The intermediate area shows laths mis-oriented from [2 2 0], as illustrated in the schematic of Fig. 10. Given the curvature of the laths it is unlikely that they conform to any single habit plane. Nonetheless, the projected width of the lath interface shows a minimum at B = [001], Fig. 9(a), and a maximum at either [1 0 1], Fig. 9(b), or [1 0 1], Fig. 9(c), where the respective {111} are in the edge orientation. The lath interface plane is parallel to [001] and therefore uniquely different from micro-twins. In fact, on rare occasions we observe laths containing some micro-twins, Fig. 11.

Fig. 7. (a) Four sets (marked as A, B, C, D) are observed. Variant A exhibits the highest density of occurrence. Energy input = 205 J, diffraction plane g = 200, B = [001]; (b) Stacking fault variant A imaged in the near edge orientation. Energy input = 205 J; g = 020; B = [101]; (c) Stacking fault variants C and D observed in the near edge orientation. Energy input = 205 J; g = 020, B = [$\bar{1}$ 0 1].

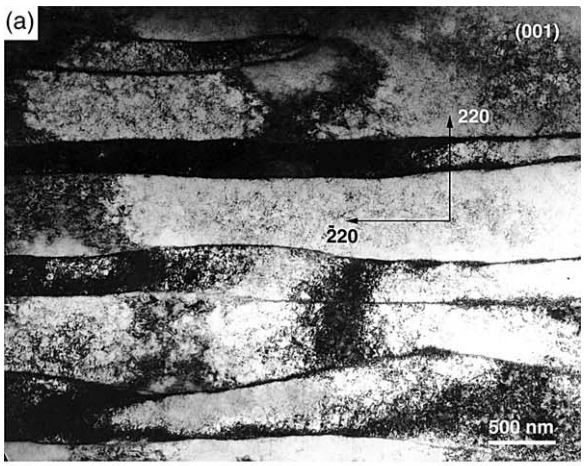

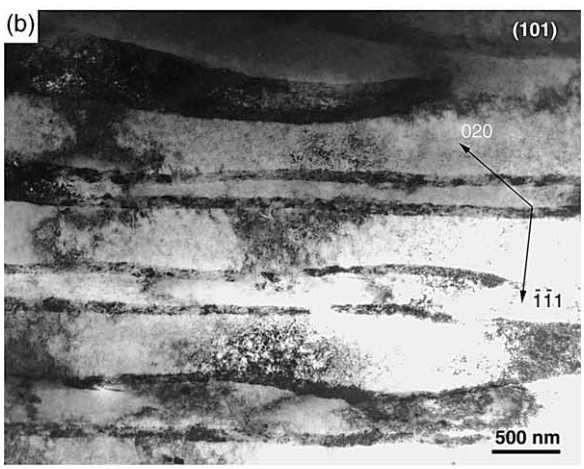

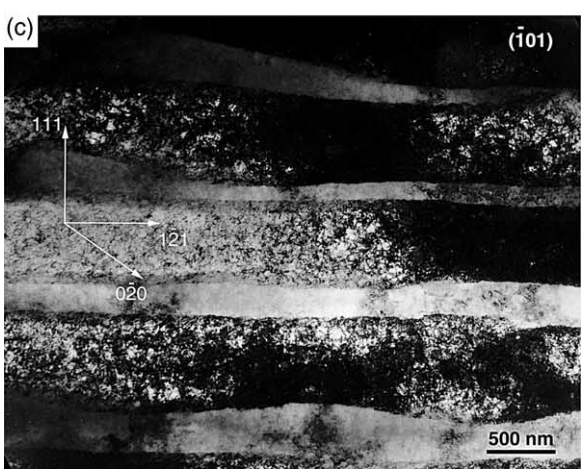

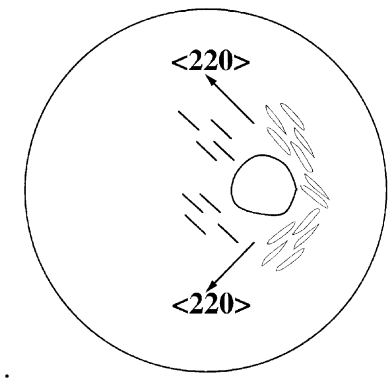

Fig. 10. Schematic of the observed variations in the deformation substructure. Note that the thin foil perforation is asymmetric with twins observed close to the center of the disc and laths observed at the edges.

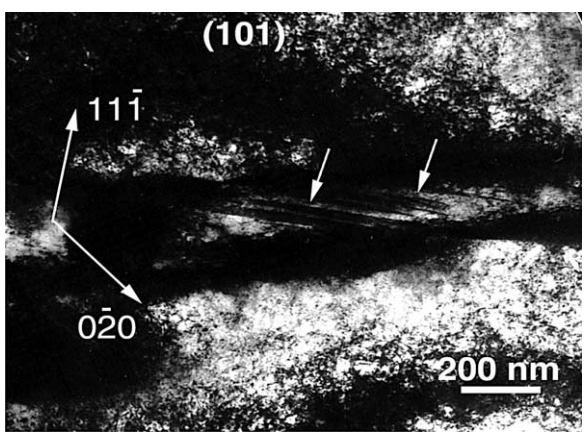

Fig. 11. Observation of micro-twins with a (1 1 $\bar{1}$) habit plane contained within laths. Energy = 320 J, g = 020, B = [101].

These features are in total agreement with the"wavy sub-grains" observed after high-pressure shock compression by Murr [18] (in particular, note similarities with Figs. 34 and 35 of [18]). This structure is also analogous to the one observed by Gray [20] in specimens where the residual strain was high. Thus, it is suggested that the substruc-

Fig. 9. (a) View of laths imaged at beam direction B = [001] with the lath interface in the near edge orientation. For (b) B = [101] and (c) B = [$\bar{1}$ 0 1] the projected width of the lath interface is larger. Thus the lath interface contains the [001] direction. The tilt sequence was imaged from B = [101] to B = [001] to B = [$\bar{1}$ 0 1].

tures revealed by Fig. 9(a)–(c) are due to thermal recovery of the shock-induced microstructure. The orientation close to {111} of the boundaries is a residue of the original twin boundaries. This microstructure represents the recovered state of a heavily twinned and dislocated structure. Fig. 12 shows the calculated shock and residual temperature rises as a function of shock pressure. The shock temperature, T_S, is a thermodynamic function of pressure, e.g. [22]. It is obtained from the Rankine–Hugoniot equations and the Grüneisen equation of state. The internal energy of the shocked material is converted into heat through the heat capacity and density:

$$T_S = \frac{(V_0 - V)}{2C_v}P + \frac{\exp[(-\gamma_0/V_0)V]}{2C_v}\int_{V_0}^{V} P\cdot\exp[(\gamma_0/V_0)V]\left[2 - \left(\frac{\gamma_0}{V_0}\right)(V_0 - V)\right]dV \quad (1)$$

V_0 and V are the initial and compressed specific volumes, respectively. γ_0 is the Grüneisen parameter for the material; P and C_v are the pressure and heat capacity, respectively. In a similar manner, the residual temperature, T_R, can be obtained from [22]:

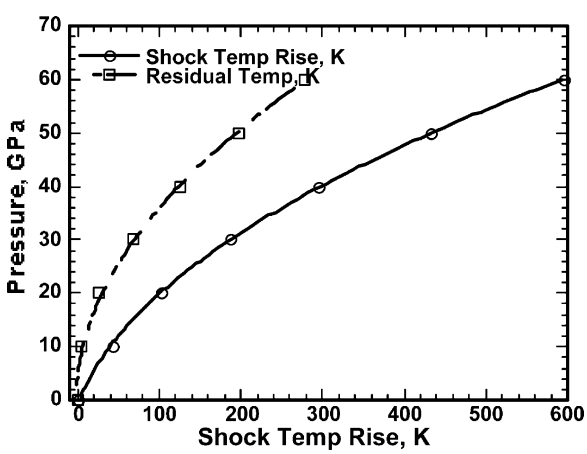

Fig. 12. Shock and residual temperature rises for copper as a function of shock pressure.

$$T_R = T_S \exp\left[\frac{\gamma_0}{V}(V_0 - V)\right] \quad (2)$$

It can be seen that the pressure of 55–60 GPa generates a residual temperature rise of 240–280 K, hence a residual temperature of 510–550 K. This is well within the recovery range for copper. Thus, the features observed are consistent with post-shock thermal recovery processes. The recovery temperature for shock-compressed copper is dependent on the shock amplitude and pulse duration. It has been established by Chojnowsky and Cahn [23]. For a duration of one minute, it is 573 K at an amplitude of 15.5 GPa and 500 K for an amplitude of 41 GPa. In the case of laser-induced shock compression, the short duration and rapid attenuation ensure a rapid temperature drop. Hence, the current results are consistent with Chojnowsky and Cahn [23].

4. Analysis

The dislocations are envisioned to be generated as loops and this is supported by Fig. 13 (two-dimensional schematic representation). The edge (positive and negative) components of the loops are shown. The sheared area (within the loop) is

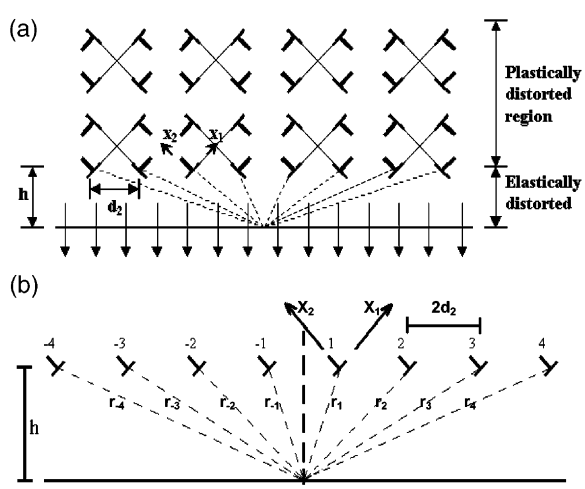

Fig. 13. (a) Stress due to dislocations on a reference point at shock front; (b) representation of one half of the first dislocation layer with distances from reference point.

indicated by a thinner line connecting the positive and negative edge dislocations. Whereas one of the loop legs moves towards the shock front, the other (opposite) is repelled from the front. Xu and Argon [24] calculated the activation energy for loop nucleation as a function of the applied shear stress using a continuum mechanics approach applying both Peierls–Nabarro [25,26], and Rice [27] potentials. The maximum shear stress σ_{12} can be related to the shock pressure P by the use of elasticity equations for uniaxial strain where ν is equal to Poisson's ratio:

$$\sigma_{12} = \left(\frac{1+\nu}{2}\right) P \tag{3}$$

The critical stress for plastic flow in Cu is given by Kelly [28]:

$$\sigma_{12} = 0.039\, G \tag{4}$$

This is taken here as the critical stress for the nucleation of loops. Thus, it is possible to convert the ratio between the shear stress and critical stress used by Xu and Argon [24] into a pressure. Their results are reproduced in Fig. 14; the shear stresses were converted into the equivalent pressure through Eq. (3).

It can be seen that the activation energy is strongly dependent on shock pressure and that it reaches a value of zero at a pressure of 3.2 GPa. Xu and Argon [24] concluded that nucleation of loops was not thermally activated in conventional plastic deformation. The activation energy is much higher than kT, the thermal energy of the atom, at the stress levels where conventional deformation takes place. In the case of shock compression, the activation energy is much lower because of the applied shear stresses due to uniaxial strain provided by the shock pressure. Hence, the formation of loops can be considered as thermally activated within the normal range of pressures used in these experiments. This fact could have an interesting effect at low temperatures, where the thermal energy of atoms (kT) is decreased. The nucleation could go through a thermal/athermal transition. Fig. 14(b) shows the portion of the plot at higher pressures. At pressures above 3–3.2 GPa, the activation energy for loop nucleation falls below the thermal energy and the nucleation would become thermally activated.

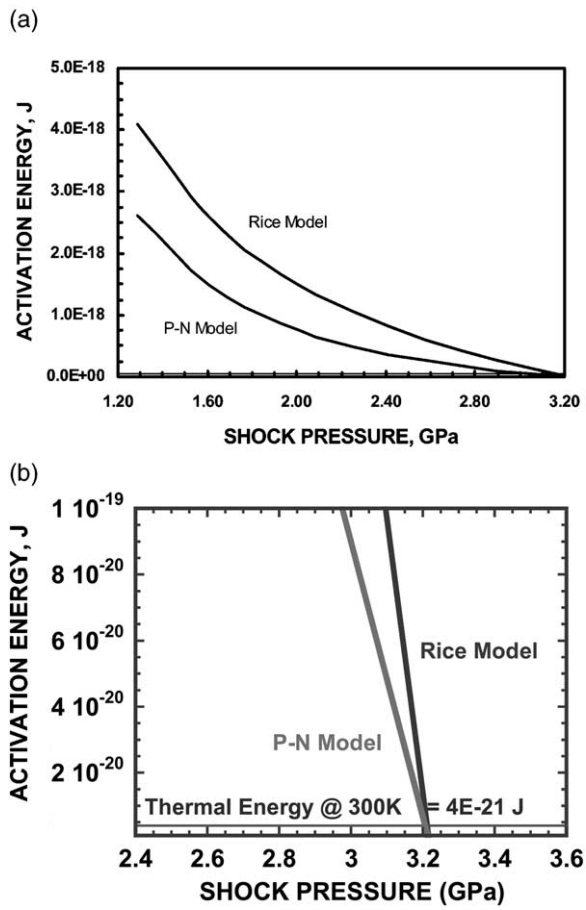

Fig. 14. (a) Activation energy for loop generation as a function of shock pressure, according to Xu and Argon [24]; (b) closeup of Fig. 14(a) showing thermal energy at 300 K and activation energies.

4.1. Shock-front distortions

Fig. 15 shows a schematic arrangement of the atomic planes that were probed, as well as their distortions for different hypothetical situations. The [100] and [010] directions, perpendicular to (200) and (020) planes, respectively, are represented in Fig. 15(a). The (020) planes are diffracted in the Bragg geometry; the incoming beam is incident on the surface opposite from the laser shock initiation. The (200) planes, that are parallel

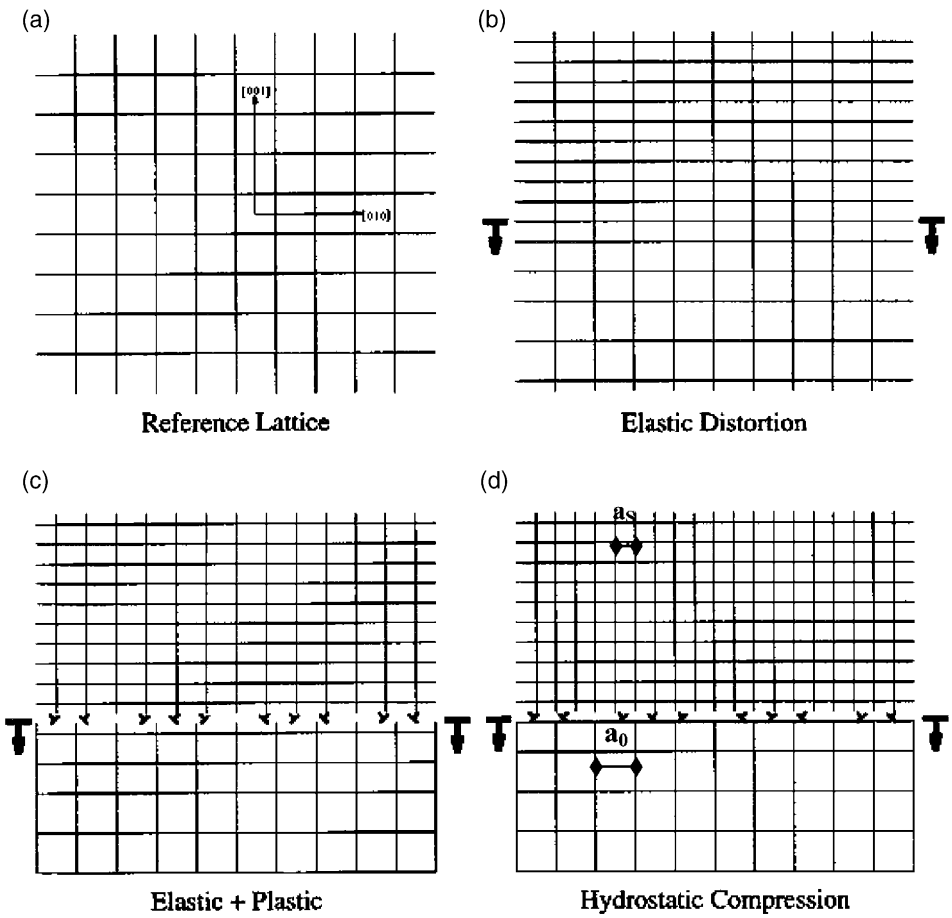

Fig. 15. Schematic representation of distortions caused in an ideal lattice oriented in an analous manner to shock experiments; (a) original configuration of planes; (b) elastic compression; (c) elastic + plastic compression with compression parallel to shock-front plane larger than perpendicular; (d) hydrostatic compression, when the compressions parallel and perpendicular are equal.

to the shock front, are imaged in the Laue geometry. The distortions in these planes can yield important information regarding the generation of defects at the shock front. If the distortion were purely elastic (Fig. 15(b)), the Laue diffraction would not show a change in angle, but the Bragg diffraction would. If there is totally hydrostatic compression, the Bragg and Laue angular changes are equal. This is shown schematically in Fig. 15(d). However, if the dislocations generated at or behind the front do not accommodate the distortion entirely, the (200) and (020) planes will exhibit different contractions, as illustrated in Fig. 15(c). Diffraction measurements from these two perpendicular planes therefore enable the determination of the distortions at the shock front. Both time integrated and time-resolved measurements were made and are shown in Fig. 16. The results shown are for the calculated pressure of 18 GPa that corresponds to a V/V_0 ratio of 0.903. If one considers a hydrostatic compression, then one has [14]:

$$\left(\frac{d}{d_0}\right)^3 = \frac{V}{V_0} \tag{5}$$

Hence, one has: $d = 0.966 d_0$. This represents approximately 3.4% change in the lattice parameter. In Fig. 16, the time-averaged changes in Bragg and Laue d spacings are 3 and 2.5%,

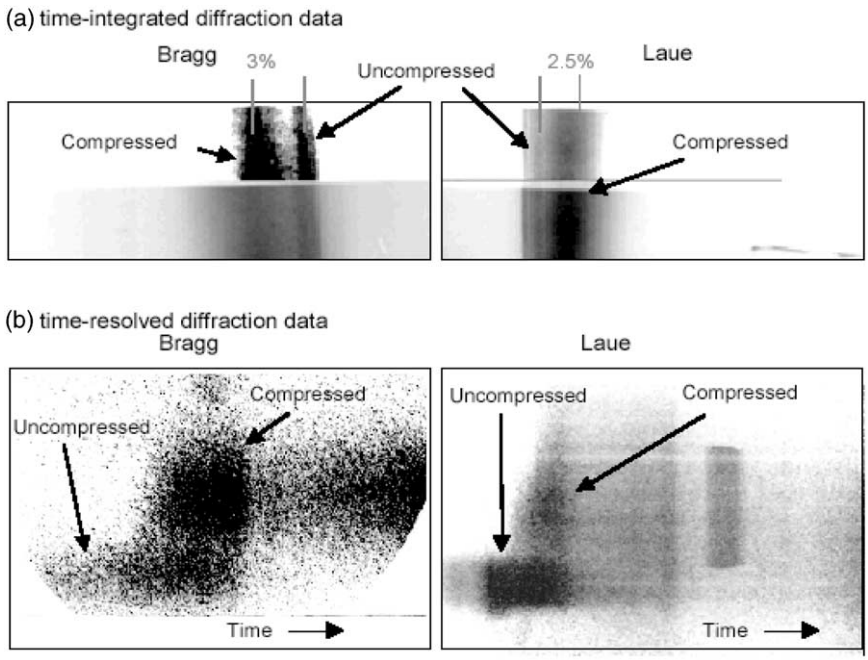

Fig. 16. Typical flash X-ray diffraction results for copper (200) and (020) planes, in Bragg (left) and Laue (right), respectively; a) time-integrated data; b) time-resolved data.

respectively. It should be mentioned that Bragg and Laue measurements were made on different specimens. Thus, the discussion below is speculative. Nevertheless, it is given because of the potential impact. These results suggest that the lattice still has considerable elastic strains stored in the Laue diffraction. The situation is analogous to the one depicted in Fig. 15(c). Thus, it is reasonable to assume that the dislocations generated do not entirely accommodate the deviatoric stresses. The deviatoric elastic distortion of the lattice can be calculated from purely elasticity considerations. If ε_1 is the strain in the [100] direction parallel to the shock front and ε_2 is the strain in the shock propagation direction [001], the shear can be expressed as:

$$\gamma = \frac{\pi}{2} - \tan^{-1}\left(\frac{1+\varepsilon_1}{1+\varepsilon_2}\right) \tag{6}$$

For infinitesimal strains: $\gamma \approx \varepsilon_1 - \varepsilon_2$ and ε_1 and ε_2 we obtained by:

$$\varepsilon_1, \varepsilon_2 = \frac{d - d_o}{d_o} \tag{7}$$

The values of d are in the [100] and [001] directions, respectively. For the present case: $\varepsilon_1 = -0.025$ and $\varepsilon_2 = -0.034$.

The flow shear stress is given by:

$$(\sigma_{12})_f = \gamma G \tag{8}$$

The shear modulus of copper is 48.36 GPa. Hence:

$$(\sigma_{12})_f \approx (\varepsilon_1 - \varepsilon_2)G = 435 \text{ MPa}$$

This value can be converted into an equivalent value for a grain size of 3 μm (the smallest size reported by Tong et al. [29]) by use of a Hall–Petch conversion. Using a Hall–Petch slope of 2.78×10^{-4} GPa $m^{-1/2}$ (from Zerilli and Armstrong [30]), one arrives at an additional stress of 45 MPa. Thus, the equivalent shear strength for a 3 μm specimen would be 480 MPa. The strain rate at the front is estimated from the strain divided by the rise time; t_f:

$$\dot{\varepsilon} = \frac{\varepsilon}{t_f} = \frac{\frac{2}{3}\ln\left(\frac{V}{V_o}\right)}{t_f} \tag{9}$$

For a pressure of 18 GPa: $\frac{V}{V_0} = 0.9$. The pulse width can be estimated at a depth of 0.05 mm from the computed profile of Fig. 2(a), which corresponds to approximately the desired pressure. It is approximately 0.025 mm thick. Taking a shock-wave velocity of 4.6 mm/μs, one obtains:

$$t_f = \frac{0.025}{4.6} = 5.4 \times 10^{-9}\ \text{s}$$

This provides a strain rate of

$$\dot{\varepsilon} = 1.3 \times 10^{7}\ \text{s}^{-1}$$

The estimated flow stress, at a strain rate of $1.3 \times 10^7\ s^{-1}$, is compared in Fig. 17 with high strain rate results by Follansbee and Gray [31] using a Kolsky–Hopkinson bar and Tong et al. [30] using a pressure-shear technique. Tong et al. [30] had to use very thin (3 μm) specimens to reach their highest strain rates. The current result obtained by flash X-ray diffraction, is consistent with an extrapolation from measurements made at lower strain rates.

It can be concluded that the result obtained herein, using flash X-ray diffraction, is consistent with the data available for copper. This illustrates the potential utility of this new method to obtain strength data in the 10^7–$10^9\ s^{-1}$ strain-rate range.

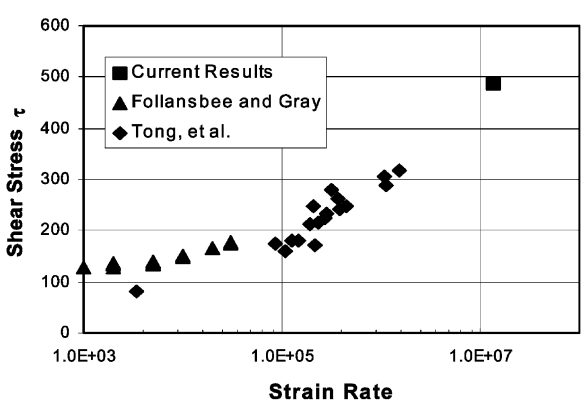

Fig. 17. Dependence of shear strength of copper on the strain rate; data by Follansbee and Gray [31], Tong et al. [29], and current estimates.

4.2. Prediction of dislocation densities

The observations made on recovered shock compressed copper specimens can be compared with analytical calculations that use physically-based mechanisms. Two aspects in particular can be predicted: the dislocation density as a function of peak shock amplitude and the threshold stress for twinning.

The first mechanism for shock-induced dislocations is due to Smith [9]. He assumed an array of edge dislocations moving with the shock front. These dislocations played a role similar to epitaxial films: they accommodated the differences in lattice parameter. Hornbogen [10] provided a significant improvement by considering edge and screw components of loops. He also considered the different mobilities of edge and screw components, determining the residual microstructure. A homogeneous dislocation nucleation mechanism was proposed by Meyers [11]. It assumes that dislocations are homogeneously generated at the front to accommodate the deviatoric stresses. In contrast with Smith's model, however, they are left behind. Weertman [12] proposed a mechanism for strong shocks using both a Smith interface and dislocations behind the front.

An improved version of the homogeneous dislocation generation mechanism [11] is described here. Fig. 13 shows an idealized configuration of dislocations when a shock wave propagates through the lattice. The dislocation planes are (111) and $(1\ 1\ \bar{1})$. The intersection of the loops with the plane perpendicular to the shock-front plane is shown in Fig. 13(a); the dislocations have edge character. As the shock front advances, the dislocation interface is left behind. As this occurs, elastic deviatoric stresses build up. The initial calculations of resulting dislocation densities produced values orders of magnitude higher than the observed results [10]. This improved calculation predicts values that compare favorably with dislocation densities measured from transmission electron microscopy observations. Successive layers of interfacial dislocation loops are generated and left behind by the shock front. The insertion of dislocations relaxes the deviatoric stresses that elastically distort an ideal cubic lattice to rhombohedral.

Hence, a reduced cubic lattice is restored by the insertion of dislocations in the vicinity near the interface. The dislocation spacing along the front required to accommodate this is d_2. This situation is analogous to the epitaxial growth of films, in which interface dislocations, creating a semicoherent boundary, accommodate the disregistry. The dislocation spacing along the front is calculated from the ratios of the original and compressed lattices. The initial and compressed specific volumes of the lattices being V_0 and V, respectively, one has:

$$\left(\frac{V}{V_0}\right)^{1/3} = \frac{a_S}{a_0} \tag{10}$$

where a_s and a_0 are the shocked and initial lattice parameters as marked in Fig. 15(d). The spacing between dislocations at the shock front (see Fig. 13a) can be expressed by the simple epitaxial dislocation equation:

$$d_2 = \frac{a_0 a_S}{a_0 - a_S} \tag{10a}$$

From Eqs. (10) and (10a), one obtains:

$$\left(\frac{V}{V_0}\right)^{1/3} = \frac{d_2}{a_S - d_2} \tag{10b}$$

For the schematic orientation shown in Fig. 15, a_S is related to the Burgers vector by:

$$b\sqrt{2} = a_S \tag{11}$$

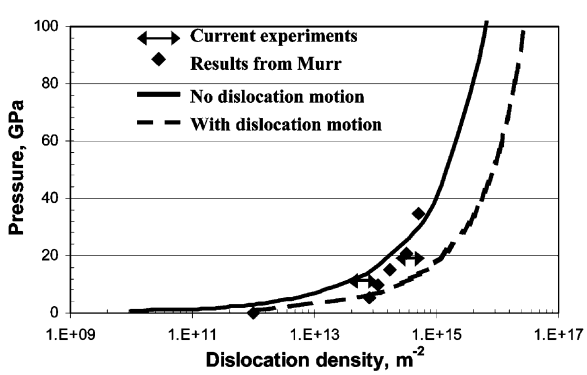

Fig. 18. Experimentally observed (from Murr [18,21] and calculated dislocation densities in copper, as a function of shock pressure.

The dislocation density generated can be calculated from d_2, the distance between dislocations at the front, and h, the spacing between successive dislocation loop layers nucleated (Fig. 13(a)). Since each distance d_2 corresponds to two dislocations (on planes (111) and $(1\,1\,\bar{1})$), the spacing $d_2/2$ is taken. Thus, the dislocation density, ρ, is:

$$\rho = \left(\frac{d_2 h}{2}\right)^{-1} \tag{12}$$

The distance between the shock-front and the first dislocation loop layer, *h*, can be calculated by using the stress fields around dislocations and summation at one point at the front over the stress field of all dislocations (Fig. 13(a).) The stress fields due to the dislocation arrays balance elastic distortion at the shock front. When the deviatoric elastic stresses at the front reach a critical level, dislocations are again generated. The stress field of an edge dislocation can be expressed as:

$$\begin{aligned}
\sigma_{11} &= \frac{Gbx_2(3x_1^2 + x_2^2)}{2\pi(1-\nu)(x_1^2 + x_2^2)^2} \\
\sigma_{22} &= \frac{Gbx_2(x_1^2 - x_2^2)}{2\pi(1-\nu)(x_1^2 + x_2^2)^2} \\
\sigma_{12} &= \frac{Gbx_1(x_1^2 - x_2^2)}{2\pi(1-\nu)(x_1^2 + x_2^2)^2}
\end{aligned} \tag{13}$$

The stress field due to a dislocation at a shock front reference position can be estimated by determining x_1 and x_2. For the front layer, the spacing between parallel dislocations is $2d_2$ for each *r* $(r_{-4}, r_{-3}, r_{-2}, r_{-1}, r_1, r_2, r_3, r_4)$ marked in Fig. 13(b) and the distance from the front is h. Hence, we have to express the coordinates of the various dislocations $x_1^{(-4)}, x_2^{(-4)}$; $x_1^{(-3)}, x_2^{(-3)}$; $x_1^{(-2)}, x_2^{(-2)}$; $x_1^{(-1)}, x_2^{(-1)}$; $x_1^{(1)}, x_2^{(1)}$; $x_1^{(2)}, x_2^{(2)}$; $x_1^{(3)}, x_2^{(3)}$; $x_1^{(4)}, x_2^{(4)}$, in terms of d_2 and h.

The stress fields of the dislocations can be expressed in terms of the distances d_2 and h by means of a transformation of axes. In the new system, $(x_1^{(1)}, x_2^{(1)})$ the ordinate is constant and equal to h, where the abscissa is equal to the $(2n + 1)d_2$, where *n* is the dislocation number (an integer ranging from $-\infty$ to ∞). This transformation yields, for dislocation 1:

$$x_1^1 = x_1^1\cos\theta + x_2^1\sin\theta = \frac{\sqrt{2}}{2}(d_2 + h)$$
$$x_2^1 = x_1^1\sin\theta + x_2^1\cos\theta = \frac{\sqrt{2}}{2}(h - d_2) \quad (14)$$

The angle of the dislocations with the shock front is taken as $\pi/2$. For the nth dislocation:

$$x_1^n = \frac{\sqrt{2}}{2}[(2n-1)d_2 + h]$$
$$x_2^n = \frac{\sqrt{2}}{2}[h-(2n-1)d_2] \quad (15)$$

These values are inserted into Eq. (13) and some simplifications are made leading to the stress field of the nth dislocation:

$$\sigma_{11}^{(n)} \sim \frac{Gb}{2\pi(1-\nu)}\frac{2\sqrt{2}}{nd_2}$$
$$\sigma_{22}^{(n)} \sim \frac{Gb}{2\pi(1-\nu)}(-2h^2)\frac{2\sqrt{2}}{n^3d_2^3} \quad (16)$$
$$\sigma_{12}^{(n)} \sim \frac{Gb}{2\pi(1-\nu)}\frac{2\sqrt{2}h}{n^2d_2^2}$$

In Eq. (16), the stresses σ_{11}, σ_{22} and σ_{12} decay with n, n^3 and n^2, respectively. In order to calculate h, the superposition principle was applied and the total stress at a point on the front due to the dislocation array is obtained by summing up the stress fields of all the dislocations. The series converge and lead to the estimate of the stresses.

$$\sum_{-\infty}^{\infty}\frac{1}{n} = 0$$
$$\sum_{-\infty}^{\infty}\frac{1}{n^3} = 0 \quad (17)$$
$$\sum_{-\infty}^{\infty}\frac{1}{n^2} = \frac{\pi^4}{90}$$

Thus:

$$\sigma_{11}^{(n)} \sim 0 \qquad \sigma_{22}^{(n)} \sim 0$$
$$\sigma_{12}^{(n)} \sim \frac{Gb}{\sqrt{2}(1-\nu)}\frac{\pi^3 h}{45d_2^2} \quad (18)$$

When the stresses at the front reach a level at which homogeneous nucleation of dislocation loops can occur, then a new layer is formed. The dislocation density can be obtained from the stress for homogeneous nucleation of dislocation loops. From Fig. 14, it is seen that the activation energy is zero at the critical stress for plastic flow given by Eq. (4). This will be considered as the stress at which the loops are generated. Substituting Eq. (4) into (18):

$$h_1 = \frac{0.8\,(1-\nu)}{b\pi^2}d_2^2 \quad (19)$$

This represents the spacing between dislocation arrays for stationary dislocations. If the dislocation is assumed to move at the shear wave velocity, under the influence of the high residual shear stresses, they try to "catch up" with the front. This results in an increase in h, given by the ratio between U_s, the shock velocity, and V_{sf}, the component of the shear wave velocity in the compressed medium. It will be assumed, to a first approximation, that the shock-wave velocity is equal to the longitudinal elastic wave velocity in an unbounded medium:

$$U_s \cong C_0 = \left(\frac{\lambda + 2\mu}{\rho_0}\right)^{1/2} \quad (20)$$

The dislocation velocity component along shock propagation direction is V_{dp}:

$$V_{dp} = \frac{\sqrt{2}}{2}C_s = \frac{1}{2}\left(\frac{2\mu}{\rho}\right)^{1/2} \quad (21)$$

ρ_0 and ρ are the initial and compressed densities, respectively (equal to $1/V_0$ and $1/V$, respectively). Thus, for dislocations traveling at the shear wave velocity:

$$h_2 = h_1\frac{C_0}{V_{dp}} = 1.6\left(\frac{1-\nu}{b\pi^2}\right)\left(\frac{V_0}{V}\right)^{1/2}\left(\frac{\lambda + 2\mu}{2\mu}\right)^{1/2}d_2^2 \quad (22)$$

The dislocation density as a function of V/V_0 is obtained by substituting Eq. (19) into Eq. (12) and Eqs. (10) and (11) into it:

$$\rho = \left(\frac{0.4\ (1-\nu)\pi^2}{\sqrt{2}\ b^2}\right)\left(1-\left(\frac{V}{V_0}\right)^{1/3}\right)^3 \tag{23}$$

The dislocation density can be expressed as a function of pressure, P, through one of the equations obtained directly from the Rankine–Hugoniot equations and the equation of state [22]:

$$P = \frac{C_0^2\left(1-\frac{V}{V_0}\right)}{V_0\left[1-S\left(1-\frac{V}{V_0}\right)\right]^2} \tag{24}$$

C_0 and S are the equation of state parameters specific to materials. Eq. (24) can be expressed as:

$$\frac{V}{V_0} = 1-\frac{1}{2PV_0S^2}[2PSV_0 + C_0^2 \pm \sqrt{(2PSV_0 + C_0^2)^2-4P^2V_0^2S^2}] \tag{25}$$

If Eq. (25) is substituted into Eq. (23) the dislocation density is directly expressed as a function of pressure. One should be careful in interpreting these results, since recovery processes occur at pressures much lower than the maximum in the plot, and these high dislocation densities are not reached. The predicted dislocation densities are plotted in Fig. 18 and compared with observations by Murr [18,21] and the currently observed results. Two configurations are shown: dislocations moving at the shear wave velocity and stationary dislocations. For the latter case, we just use Eq. (19), which is substituted into Eqs. (12) and (10), and then into Eq. (24). This is given by:

$$P = \frac{C_0^2\left\{1-\left\{1-\sqrt{2}\left[\frac{0.8\ b^2(1-\nu)\rho}{2\pi^2}\right]^{1/3}\right\}^3\right\}}{V_0\left\{1-S\left\{1-\sqrt{2}\left[\frac{0.8\ b^2(1-\nu)\rho}{2\pi^2}\right]^{1/3}\right\}^3\right\}^2} \tag{26}$$

The results presented in Fig. 18 are encouraging, since the calculated densities "bracket " the experimental results. This approach can lead to realistic prediction of dislocation densities.

4.3. Prediction of threshold amplitude for twinning

The methodology to be used in the prediction of the threshold shock amplitude for twinning was delineated by Murr et al. [32] and Meyers et al. [33]. The procedure presented herein can be used to predict the critical pressure for twinning in shock compression experiments. It is known that different metals have different threshold pressures for the initiation of twinning; it has been established by Murr [34] that this pressure is a function of stacking-fault energy, for FCC metals. Slip and twinning are considered as competing mechanisms; whereas plastic deformation by slip has a strain rate and temperature dependence well described by the theory of thermally-activated obstacles, it is assumed that the strain rate and temperature dependence for slip are much lower. This is corroborated by experimental evidence presented in Section 3. Setting $\sigma_T = \sigma_s$, one can obtain the critical twinning stress as a function of ε, $\dot{\varepsilon}$, and T. The application of this criterion to the shock front necessitates the knowledge of the strain rate. The strain rate at the shock front has been established by Swegle and Grady [35] to be:

$$P = k_{SG}\dot{\varepsilon}^{1/4} \tag{27}$$

Fig. 19 shows a Swegle–Grady plot in which the axes were normalized in order to provide a better superposition of data. The data has not entirely collapsed onto a single line, but the scatter is reduced. One could, to a first approximation, define a single k_{SG} parameter.

Two separate aspects have to be considered in

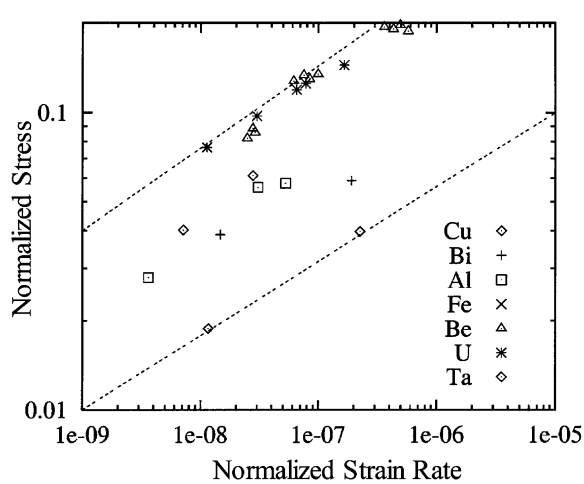

Fig. 19. Modified Swegle–Grady plot with normalized axes (Adapted from Swegle and Grady [35]).

the analysis: (a) shock heating and (b) plastic strain at the shock front. Both shock heating and plastic strain by slip (and associated work hardening) alter the flow stress of material by slip processes and need to be incorporated into the computation. The total (elastic + plastic) uniaxial strain, ϵ, at the shock front is related to the change in specific volume by:

$$\frac{V}{V_0} = e^{\varepsilon} \tag{28}$$

Inserting Eq. (28) into Eq. (24), we obtain:

$$P = \frac{C_0^2(1-e^{\varepsilon})}{V_0[1-S(1-e^{\varepsilon})]^2} \tag{29}$$

The constitutive response of the copper monocrystal is represented by the modified MTS expression below; the parameters are taken from Follansbee and Gray [31]. A modified MTS equation is used, with values of p = 1/2 and q = 3/2, respectively [36]. The value of g_0 is 0.8 [36].

$$\sigma = \sigma_0 f(\varepsilon)\left[1-\left(\frac{kT}{Gb^3 g_0} Ln\left(\frac{\dot{\varepsilon}_0}{\dot{\varepsilon}}\right)\right)^{2/3}\right]^2 \tag{30}$$

The work hardening (f(ε)) was incorporated by taking a polynomial representation of the stress strain curve for a single crystal. This crystal is shown in Fig. 16(a) of Meyers et al. [33]. This orientation is the closest to [100], which has the lowest threshold pressure for twinning. This polynomial is:

$$f(\varepsilon) = 45510\,\varepsilon^6 - 86899\,\varepsilon^5 + 63406\varepsilon^4 - 21834\varepsilon^3 + 2901.8\varepsilon^2 + 464.8\varepsilon^1 - 1.92 \tag{31}$$

The grain size effects were incorporated by adding a Hall–Petch term to Eq. (30). The procedure used in calculating the threshold stress is to obtain a first estimate of the threshold pressure:

$$\sigma_T = \sigma_s \tag{32}$$

The normal twinning stress (σ_T) used in this calculation was 490 MPa [37]. Eq. (32) is applied to Eq. (30), at a low value of plastic strain. The value of the strain rate obtained from this is then fed into Eq. (27). This provides a first estimate of the pressure, P. This pressure is then used to calculate the shock strain and temperature through Eqs. (29) and (2), respectively. These values are then fed back into Eqs. (27)–(32) and a second pressure is calculated. This iterative process converges to the critical twinning stress. Fig. 20 shows the application of this method to copper. The plot shows how the initial temperature and grain size affect the threshold shock pressure. There is a significant increase in the threshold stress when the grain size is decreased from 10 mm to 1 μm. The shock temperature has a small effect on the threshold pressure. The calculated threshold pressure for a monocrystal (modeled by a 10 mm grain size) shocked from an initial temperature of 300 K is 17 GPa. This compares favorably with experimental results by De Angelis and Cohen [15]: 14 GPa. This approach, which was not optimized here, yields results that are close to actual observations. They represent the first prediction of twinning threshold in shock compression. It is expected that in the near future we will be able to predict the effect of other microstructural parameters, such as the stacking-fault energy, especially the twinning threshold, and substructures generated in shock compression.

5. Conclusions

It is demonstrated that laser-driven shock compression experiments can provide unique information on the processes of defect generation at high strain rates. The results indicate that all criti-

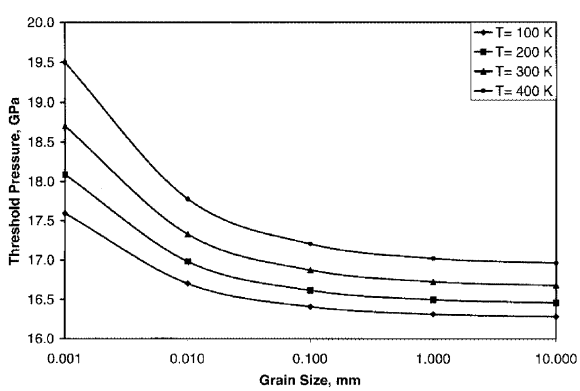

Fig. 20. Threshold shock pressure for twinning in copper as a function of grain size at different initial temperatures (100, 200, 300 and 400 K).

cal processes of defect generation operate at the shock front. The pulse duration in the current experiments was on the order of nanoseconds, two orders of magnitude lower than plate impact experiments. Nevertheless, the substructures observed by transmission electron microscopy are very similar. The experimental results are compared with analytical predictions that enable the calculation of the dislocation density as a function of pressure, as well as the threshold pressure for mechanical twinning. The predicted results compare favorably with experimental observations.

Acknowledgements

Research supported by the Department of Energy Grants DEFG0398DP00212 and DEFG0300SF2202, and by the US Army Research Office MURI Program.

References

[1] Askaryon GA, Morez EM. JETP Lett 1963;16:1638.
[2] Anderholm NC. Appl Phys Lett 1970;12:113.
[3] Fairand BP, Clauer AH, Jung RG, Wileot BA. Appl Phys Lett 1974;25:431.
[4] Clauer AH, Holbrouk JH, Fairand BP. In: Meyers MA, Murr LM, editors. Shock waves and high-strain-rate phenomena in metals. NY: Plenum; 1981. p. 67-5.
[5] Johnson Q, Mitchell A, Keeler RN, Evans L. Phys Rev Lett. 1970;25:109.
[6] Zaretsky E. J Appl Phys 1995;78:1.
[7] Wark JS et al. Phys Rev B 1989;40:5705.
[8] Kalantar DH, Chandler EA, Colvin JD, Lee R, Remington BA, Weber SV, Hauer A, Wark JS, Loveridge A, Failor BH, Meyers MA, Ravichandran G. Rev Sci Instr 1999;170:629.
[9] Smith CS. Trans AIME 1958;212:574.
[10] Hornbogen E. Acta Met 1962;10:978.
[11] Meyers MA. Scripta Met 1978;12:21.
[12] Weertman J. Mech of Matls 1986;5:13.
[13] Johnson J. Micromechanical strength effects in shock compression of solids. In: High pressure science and technology—1993. NY: AIP, 1994 p. 1145.
[14] Meyers MA, Murr LE. In: Shock waves and high-strain-rate phenomena in metals. NY: Plenum; 1981. Appendices.
[15] De Angelis RJ, Cohen JB. J. of Metals 1963;15:681.
[16] Nolder RL, Thomas G. Acta Met. 1963;11:994.
[17] Nolder RL, Thomas G. Acta Met 1964;12:227.
[18] Murr LE. In: Meyers MA, Murr LE, editors. Shock waves and high-strain-rate phenomena in metals. NY: Plenum; 1981. p. 60-7.
[19] Grace FI. J Appl Phys 1969;40:2649.
[20] Gray III GT. In: Meyers MA, Murr LE, Staudhammer KP, editors. Shock-wave and high-strain-rate phenomena in materials. NY: M. Dekker; 1992. p. 89-9.
[21] Murr LE. Scripta Met 1978;12:201.
[22] Meyers MA. Dynamic behavior of materials. NY: J. Wiley, 1994.
[23] Chonovsky EA, Cahn RW. In: Rohde R, editor. Metallurgical effects at high strain rates. 1973. p. 63-1.
[24] Xu G, Argon AS. Phil Mag Lett 2000;80:605.
[25] Peierls RE. Proc Phys Soc 1940;52:23.
[26] Nabarro FRN. Proc Phys Soc 1947;59:256.
[27] Rice JR. J Mech Phys Solids 1992;40:239.
[28] Kelly A. Strong solids. 2nd ed. Oxford: Clarendon Press, 1973.
[29] Tong W, Clifton RJ, Huang S. J Mech Phys Sol 1992;40:1251.
[30] Zerilli FJ, Armstrong RW. J Appl Phys 1987;61:1816.
[31] Follansbee PS, Gray III GT. Matls Sci and Eng 1991;138:23.
[32] Murr LE, Meyers MA, Niou C-S, Chen Y-J, Pappu S, Kennedy C. Acta Mater 1997;45:157.
[33] Meyers MA, Benson DJ, Voehringer O, Kad BK, Xue Q, Fu H-H. Matls Sci and Eng 2002, in press.
[34] Murr LE. In: Schmidt SC, Holmes NC, editors. Shock waves in condensed matter. Amsterdam: Elsevier; 1988. p. 31-5.
[35] Swegle JW, Grady DE. J Appl Phys 1983;58:941.
[36] Follansbee PS. In: Murr LE, Staudhammer KP, Meyers MA, editors. Metallurgical applications of shock-wave and high-strain rate phenomena. M. Dekker; 1986. p. 45-1.
[37] Meyers MA, Voehringer O, Lubarda VA. Acta Mat 2001;49:4025.